Multifractal subgrid-scale modeling for large-eddy simulation. I. Model development and *a priori* testing

Gregory C. Burton[a)]
Laboratory for Turbulence and Combustion and W. M. Keck Laboratory for Computational Fluid Dynamics, Department of Aerospace Engineering, The University of Michigan, Ann Arbor, Michigan 48109-2140

Werner J. A. Dahm
Laboratory for Turbulence and Combustion (LTC), Department of Aerospace Engineering, The University of Michigan, Ann Arbor, Michigan 48109-2140

(Received 27 April 2005; accepted 13 May 2005; published online 13 July 2005)

Results are presented from a new approach to modeling the subgrid-scale stresses in large-eddy simulation of turbulent flows, based on explicit evaluation of the subgrid velocity components from a multifractal representation of the subgrid vorticity field. The approach is motivated by prior studies showing that the enstrophy field exhibits multifractal scale-similarity on inertial-range scales in high Reynolds number turbulence. A scale-invariant multiplicative cascade thus gives the spatial distribution of subgrid vorticity magnitudes within each resolved-scale cell, and an additive cascade gives the progressively isotropic decorrelation of subgrid vorticity orientations from the resolved scale Δ to the viscous scale λ_ν. The subgrid velocities are then obtained from Biot–Savart integrals over this subgrid vorticity field. The resulting subgrid velocity components become simple algebraic expressions in terms of resolved-scale quantities, which then allow explicit evaluation of the subgrid stresses τ_{ij}^*. This new multifractal subgrid-scale model is shown in *a priori* tests to give good agreement for the filtered subgrid velocities, the subgrid stress components, and the subgrid energy production at both low ($Re_\Delta \approx 160$) and high ($Re_\Delta \approx 2550$) resolved-scale Reynolds numbers. Implementing the model is no more computationally burdensome than traditional eddy-viscosity models. Moreover, evaluation of the subgrid stresses requires no explicit differentiation of the resolved velocity field and is therefore comparatively unaffected by discretization errors. © *2005 American Institute of Physics*. [DOI: 10.1063/1.1965058]

I. INTRODUCTION

Large-eddy simulation (LES) in principle allows for significantly improved accuracy in simulating turbulent flows, by calculating the large-scale features of the flow while modeling the small scales. Since the large scales are unique to each flow, representing them with any universal turbulence model, as in traditional Reynolds-averaged modeling, is inherently problematic. The small scales of turbulent flows, on the other hand, become increasingly universal with progressively decreasing scale size, and are significant insofar as the flow itself is concerned only for their cumulative effect on the evolution of the large scales. Interactions between the large (resolved) scales and the small (unresolved) scales are accounted for by a subgrid-scale model.

Despite this promising framework, however, LES has yet to fulfill the role which its original proponents had intended.[1] In the 40 years since the development of the first practical subgrid-scale model by Smagorinsky,[2] LES approaches and subgrid-scale models have been proposed with some frequency, yet none has achieved the accuracy necessary for LES to become the preferred turbulence modeling method for the practicing engineer and scientist. While the past 15 years have seen modest improvements in LES techniques as well as application of LES to more complex flow regimes,[3] much of this apparent progress has resulted from the use of increasingly powerful computers, rather than from improvements to the underlying models and numerical methods. Since computer power will not increase fast enough to permit practical direct simulation of most turbulent flows for the foreseeable future,[4] further near-term advances in turbulent flow simulation must necessarily require improvements in turbulence modeling methods. Thus, development of accurate yet computationally efficient subgrid-scale models and related numerical techniques remain one of the central problems that must be solved to make LES a reliably accurate tool for a wide range of practical turbulent flow problems.

A. The subgrid stress tensor τ_{ij}

Large-eddy simulations commonly solve a form of the filtered momentum equation which, under incompressibility and commutivity of the filtering and derivative operators, can be written as

$$\frac{\partial \bar{u}_i}{\partial t} + \frac{\partial}{\partial x_j}\bar{u}_i\bar{u}_j + \frac{1}{\rho}\frac{\partial \bar{p}}{\partial x_i} - \nu\frac{\partial^2 \bar{u}_i}{\partial x_j} = -\frac{\partial}{\partial x_j}\tau_{ij}, \tag{1}$$

with the subgrid stress tensor τ_{ij} defined as

[a)]Present address: Center for Turbulence Research, Stanford University, Stanford, CA 94305-3035.

$$\tau_{ij} = \overline{u_i u_j} - \bar{u}_i \bar{u}_j, \tag{2}$$

and with the overbar representing an explicit or implicit filter at scale Δ that defines the large scales of the flow. The form of the filtered momentum equation in (1) is most widely used because it involves material derivatives of the resolved momentum, permitting use of traditional Navier–Stokes codes. The subgrid interactions are isolated in τ_{ij}, which must be modeled.

While any errors in modeling τ_{ij} necessarily introduce inaccuracies in momentum transport within the flow, simulations at a minimum seek to transport kinetic energy with reasonable accuracy in the resolved scales. The equation for the resolved kinetic energy $\frac{1}{2}\bar{u}_i\bar{u}_i$, obtained by multiplying (1) by $\bar{u}_i$, leads to a subgrid energy production term $\mathcal{P} \equiv -\tau_{ij}\bar{S}_{ij}$ that accounts for the transfer of energy between the resolved and subgrid scales due to interaction of the subgrid stress τ_{ij} with the resolved strain rate $\bar{S}_{ij}$. A key goal in subgrid-scale modeling of τ_{ij} is to accurately capture the resulting forward ($\mathcal{P}>0$) and backward ($\mathcal{P}<0$) transfer of energy represented by the subgrid energy production field $\mathcal{P}(\mathbf{x},t)$.

B. Previous models for τ_{ij}

Subgrid-scale models for τ_{ij} can be broadly grouped into "functional" and "structural" approaches.[5] In general, functional models seek only to reproduce the net kinetic energy transfer from the resolved to the subgrid scales during a simulation; they are "physical models" only in that they mimic the average energy cascade from the large to the small scales, as first noted by Richardson.[6] The most widely used functional models are eddy-viscosity formulations, in which the subgrid stress is assumed proportional to the resolved strain rate $\bar{S}_{ij}$ through an eddy-viscosity modeled as $\nu_t \approx C_s\Delta^2|\bar{S}|$, as first proposed by Smagorinsky.[2] A number of modifications to the Smagorinsky model have been proposed, most focused on better estimating the eddy-viscosity parameter C_s. Germano *et al.*[7] introduced a dynamic model based on double-filtering of the resolved velocity field to allow local determination of C_s throughout the simulation. Various other adaptive[8–11] as well as spectral[12,13] eddy-viscosity approaches have been explored. A hallmark of nearly all functional models is that they cannot reproduce the local instantaneous stress $\tau_{ij}(\mathbf{x},t)$ and energy-production $\mathcal{P}(\mathbf{x},t)$ fields, but nevertheless produce stable simulations, if the net energy is drawn out at approximately the correct rate.

By contrast, structural models seek to recover actual structures of the subgrid field that influence the evolution of the resolved scales. As such, these methods hold the promise of higher fidelity LES, since it has been long understood that flow structures near the filter cut-off scale strongly influence the transport of momentum and energy across the LES filter boundary, and hence exert a significant influence on the evolution of the resolved scales.[12] The scale-similarity model of Bardina *et al.*[14,15] is a structural approach that calculates the subgrid stresses by an assumed equivalence between the smallest resolved and largest unresolved scales as $\tau_{ij} \sim \overline{\bar{u}_i\bar{u}_j} - \bar{u}_i\bar{u}_j$. While the modeled stresses correlate well with filtered DNS values, the average subgrid energy production $\mathcal{P}$ is too low, and the model is thus typically combined with an eddy-viscosity model to give a "mixed" model. Zang *et al.*[16] used a local dynamic modification of the eddy-viscosity coefficient in the mixed model. Brasseur and Wei[17] proposed a spectral model based on the dynamics of triadic interactions among local, nonlocal and distant Fourier modes. The inverse approach of Guerts[18] attempts to recover the subgrid velocity field from the resolved field with an approximate higher-order polynomial inversion of the spatial filter, and the approximate deconvolution procedure of Stoltz and Adams[19] similarly employs an approximate inverse of the filter to obtain a representation of the subgrid velocity field, which is then used to calculate τ_{ij}. The velocity-estimation approach, proposed by Domaradzki[20,21] in spectral and physical-space versions, is a two-step method involving deconvolution and nonlinear evolution to approximate the velocity field at the scale $\Delta/2$, which is then used to calculate the subgrid stress τ_{ij} directly. Scotti and Meneveau[22] estimate τ_{ij} from a subgrid velocity field constructed using fractal interpolation, involving an iterative mapping in one dimension that interpolates velocities between points on the resolved grid assuming time-series traces of the velocity field are fractal.

Also relevant to the present approach are several models based on the subgrid vorticity field. Pullin and Saffman[23] proposed a vortex-structure model that approximates subgrid-scale turbulent structures as straight, rodlike cylinders of vorticity, allowing a partly stochastic representation of τ_{ij}, and Misra and Pullin[24] have evaluated specific forms of these stochastic functions. LES schemes for the vorticity transport equation have been proposed by Mansfield *et al.*[25] based on a Lagrangian eddy-viscosity approach, and by Farge *et al.*[26] based on a coherent-vortex method.

C. The subgrid stress tensor τ^*_{ij}

An alternative to (1) and (2) is to decompose the velocity $\mathbf{u}(\mathbf{x},t)$ into resolved and subgrid components as $\mathbf{u} \equiv \bar{\mathbf{u}} + \mathbf{u}^{sgs}$, and then write the subgrid stress in (2) as

$$\tau_{ij} = \tau^R_{ij} + \tau^*_{ij}, \tag{3}$$

where

$$\tau^R_{ij} \equiv \overline{\bar{u}_i\bar{u}_j} - \bar{u}_i\bar{u}_j, \tag{4}$$

$$\tau^*_{ij} \equiv \overline{\bar{u}_i u^{sgs}_j} + \overline{u^{sgs}_i \bar{u}_j} + \overline{u^{sgs}_i u^{sgs}_j}. \tag{5}$$

From (3)–(5) it is apparent that τ_{ij} includes a part τ^R_{ij} that does not involve the subgrid velocity field at all, and a part τ^*_{ij} that includes all the contributions from the subgrid velocity field. In principle τ^R_{ij} can be evaluated from the resolved velocity field, however, on substituting (3) into (1) the filtered momentum equation can be written as

$$\frac{\partial \bar{u}_i}{\partial t} + \frac{\partial}{\partial x_j}\overline{\bar{u}_i\bar{u}_j} + \frac{1}{\rho}\frac{\partial \bar{p}}{\partial x_i} - \nu\frac{\partial^2 \bar{u}_i}{\partial x_j} = -\frac{\partial}{\partial x_j}\tau^*_{ij}, \tag{6}$$

where only the subgrid part of the stress tensor τ^*_{ij} now appears.[27–30] This form of the momentum equation avoids the need to explicitly evaluate τ^R_{ij} in (4), but does require

explicit filtering of the product $\bar{u}_i\bar{u}_j$ in the inertial term in (6), as well as a subgrid-scale model for τ_{ij}^*.

With regard to energy transfer between the resolved and subgrid scales implied in the momentum equation in (6), the subgrid energy production is $\mathcal{P}=\mathcal{P}^*+\mathcal{P}^R$, where $\mathcal{P}^* \equiv -\tau_{ij}^*\bar{S}_{ij}$, and $\mathcal{P}^R \equiv -\overline{\bar{u}_i\bar{u}_j}\bar{S}_{ij}$. Note that the contribution of $\mathcal{P}^R(\mathbf{x},t)$ to the resolved-scale energetics is implicitly accounted for in (6), and is not directly affected by the subgrid-scale modeling for τ_{ij}^*. The τ_{ij}^* model instead directly contributes to energy exchange between the resolved and subgrid scales only through $\mathcal{P}^*(\mathbf{x},t)$.

D. Present approach

Each of the terms in the subgrid stress τ_{ij}^* in (5) can be evaluated from a structural model that provides the subgrid velocity component fields u_i^{sgs} throughout each grid cell from the resolved fields. Here we propose such a model for τ_{ij}^* based on the structure of the subgrid vorticity field $\boldsymbol{\omega}^{sgs}$ over inertial-range scales, from which the resulting subgrid velocity field can then be obtained from the Biot–Savart integral

$$\mathbf{u}^{sgs}(\mathbf{x},t) \equiv \frac{1}{4\pi}\int_{\mathbf{x}'} \boldsymbol{\omega}^{sgs}(\mathbf{x}',t) \times \mathbf{K}(\mathbf{x},\mathbf{x}')d^3\mathbf{x}', \tag{7}$$

where

$$\mathbf{K}(\mathbf{x},\mathbf{x}') \equiv \frac{\mathbf{x}-\mathbf{x}'}{|\mathbf{x}-\mathbf{x}'|^3}. \tag{8}$$

Since much is known about the structure of the vorticity field at intermediate and small scales in high Reynolds number turbulent flows, this provides a rational basis for representing the subgrid vorticity field in a model for τ_{ij}^*. Moreover, the integral nature of the Biot–Savart law in (7) that determines the subgrid velocity field from this subgrid vorticity field renders the resulting velocities inherently less sensitive to the precise details of the modeled subgrid vorticity.

The model developed here builds on many of the earlier models noted in Sec. I B (e.g., Refs. 17, 20, and 21), as well as other studies[31–33] which have shown that gradient fields such as the enstrophy in turbulent flows obey multifractal scale-similarity over inertial-range scales. This multifractal subgrid-scale structure in the enstrophy field can thus be represented by a multiplicative cascade that distributes the total subgrid enstrophy, determined from its equilibrium inertial-range scaling, within each resolved-scale grid cell Δ. An additive cascade gives the decorrelation of subgrid vorticity orientations at successively smaller scales from the orientation at the grid-scale Δ. The Biot–Savart integral in (7) is then evaluated from this subgrid vorticity field ω_i^{sgs} to give the expectation value of each of the subgrid velocity component fields u_i^{sgs}. These in turn allow direct evaluation of the subgrid stress tensor τ_{ij}^* in (5) and (6).

Here we derive this multifractal subgrid-scale model and present results from *a priori* comparisons between the model and direct numerical simulation (DNS) data for (i) the filtered subgrid velocity fields $\overline{u_i^{sgs}}(\mathbf{x},t)$, (ii) the subgrid stress components fields $\tau_{ij}^*(\mathbf{x},t)$, and (iii) the subgrid-energy production field $\mathcal{P}^*(\mathbf{x},t)$ at both low and high filter-scale Reynolds numbers. The resulting multifractal model is no more computationally taxing than the dynamic eddy-viscosity models discussed above, yet will be seen here to capture the principal features of both momentum and energy transfer in large-eddy simulation of turbulent flows. A companion paper[34] demonstrates that stable and accurate large-eddy simulations can be obtained with this multifractal subgrid-scale model for τ_{ij}^* when solving the form of the filtered momentum equation in (6).

II. MULTIFRACTAL FIELDS

Detailed treatments of the multifractal formalism are given by Falconer[35] and Peitgen *et al.*;[36] here we review only those aspects of multifractal scale-similarity that are essential for the present subgrid-scale model.

A. Multiplier distribution $P(\mathcal{M})$

Multifractal fields result from the repeated application of a scale-invariant multiplicative process to an initial field. In turbulent flows, such a multiplicative process is provided by the continual stretching and folding action of the time-varying strain rate and vorticity fields, with the required scale-invariance being naturally satisfied for scales sufficiently removed from boundaries. Such scale-invariant multiplicative processes can be represented by deterministic or stochastic multiplicative cascades, in which a scale-invariant distribution of multipliers $\mathcal{M}$ maps the field of interest from one iteration to the next as the cascade proceeds. In one-dimensional stochastic binomial cascades, for example, at each stage of the construction the quantity of interest μ contained in any given cell is distributed over two cells, each half the size of the previous stage, with the multiplier $\mathcal{M}$ that determines the division between the cells determined randomly from a scale-invariant distribution $P(\mathcal{M})$. After a sufficient number $\mathcal{N}$ of such repetitions, the resulting one-dimensional field $\mu(x)$ given by

$$\mu(x) = \mu_0(x)2^{\mathcal{N}}\prod_{n=1}^{\mathcal{N}} \mathcal{M}_n(x) \tag{9}$$

becomes highly intermittent and displays multifractal scaling properties.

The multiplier distribution $P(\mathcal{M})$ which underlies a multifractal field can be used to generate synthetic fields that, over the range of scales at which the scale-invariant similarity applies, are statistically indistinguishable from the original field. It is this fact that forms the basis for the multifractal subgrid-scale model developed in Sec. III. Owing to the stochastic nature of the cascade process, arbitrarily many different realizations of the field $\mu(\mathbf{x},t)$ can be produced from the same $P(\mathcal{M})$. Each such field differs in detail, but has the same multiplicative scale-similarity properties. The scale-invariance in the underlying multiplier distribution leads to power-law scalings in partition functions associated with the field, and moments of the resulting fields are determined entirely by the multiplier distribution $P(\mathcal{M})$.

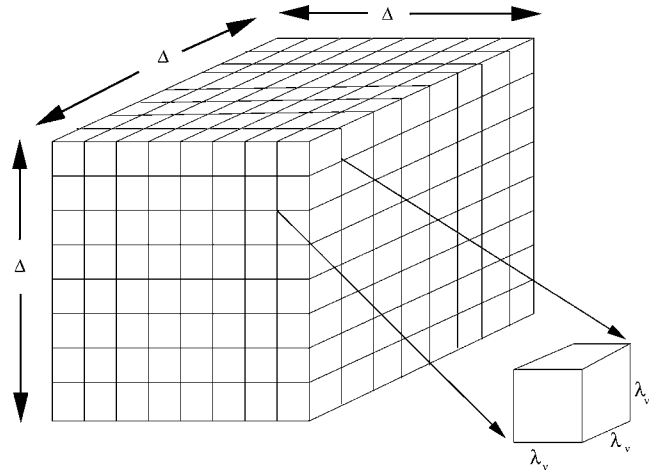

FIG. 1. Schematic representation of the $N \equiv (\Delta/\lambda_\nu)^3$ inner-scale cells of size λ_ν comprising the subgrid vorticity field $\boldsymbol{\omega}^{sgs}$ within each resolved-scale grid cell of size Δ; separate cascades distribute values for the subgrid enstrophy and subgrid vorticity orientation to each inner-scale cell.

B. Multifractal structure in turbulent flows

Fundamental considerations suggest that gradient-magnitude fields in turbulent flows, such as the enstrophy, the kinetic energy dissipation rate, and the scalar energy dissipation, will display multifractal scale-similarity as a result of the repeatedly applied stretching and folding action of the space- and time-varying strain rate and vorticity fields. Experimental studies by Meneveau and Sreenivasan[31,32] have indeed shown that the energy dissipation rate field exhibits multifractal scaling, and Meneveau[37] subsequently also found results consistent with multifractal scaling from wavelet analyses of the dissipation field. Sreenivasan and Stolovitzky[38] further examined scale similarity in turbulent flows and suggested the possibility of correlations in the cascade process. Similarly, experimental investigations by Prasad *et al.*,[39] Sreenivasan and Prasad,[40] and Frederiksen *et al.*[41,42] have further verified that scalar energy dissipation rate fields in turbulent flows display multifractal scale similarity as well.

The scale-invariant cascade process that leads to multifractal fields can also be applied "in reverse" to test for multifractal scale-similarity based on scale-invariance in the multiplier distribution, as first proposed by Sreenivasan[33] and Chhabra and Sreenivasan.[43] The original field is used to obtain a multiplier distribution $P(\mathcal{M}_\varepsilon)$ at each scale ε by computing the multipliers $\mathcal{M}_\varepsilon$ between successive scales at every point. If the field is multifractal, then the resulting $P(\mathcal{M}_\varepsilon)$ at each scale ε will be scale invariant. Frederiksen *et al.*[41,42] have used this procedure to establish within rigorous statistical bounds that scalar gradient fields in turbulent flows display multifractal scale similarity. This procedure was also used to investigate enstrophy and dissipation fields for multifractal scale invariance in DNS of homogeneous, isotropic turbulence by Burton[44] and in direct experimental measurements of enstrophy and dissipation in turbulent shear flows by Mullin and Dahm.[45] Of particular relevance to the present subgrid-scale model, those studies have both directly confirmed multifractal structure in the enstrophy field over inertial-range scales. Collectively, these experimental and computational results provide the basis for a multifractal subgrid-scale model for τ^*_{ij}.

III. MULTIFRACTAL MODELING OF τ^*_{ij}

The subgrid-scale model for τ^*_{ij} presented here is based on constructing a subgrid-vorticity field ω_i^{sgs} within each resolved-scale grid cell via a multiplicative cascade of the type in Sec. II, beginning at the grid scale Δ and continuing down to the inner (viscous) length scale λ_ν, as indicated in Fig. 1. Separate cascades distribute the vorticity magnitudes $|\boldsymbol{\omega}^{sgs}|$ and orientations $\hat{\mathbf{e}}^{sgs}$ to each of the inner-scale cells. A multiplicative cascade based on the scale-invariant multiplier distribution $P(\mathcal{M})$ for the enstrophy field determines the vorticity magnitude $|\boldsymbol{\omega}^{sgs}|$ in each such cell as in (9). An additive cascade similarly determines the spatial distribution of the subgrid vorticity orientations $\hat{\mathbf{e}}^{sgs}$ in each inner-scale cell. Both cascades remain sensitive to the filter-scale Reynolds number Re_Δ, since the number of iterations

$$\mathcal{N} \equiv \log_2(\Delta/\lambda_\nu) \tag{10}$$

in each cascade is determined by the grid-scale to inner-scale ratio $(\Delta/\lambda_\nu) \sim Re_\Delta^{3/4}$. This is illustrated in Fig. 2, which schematically shows one-dimensional intersections through the

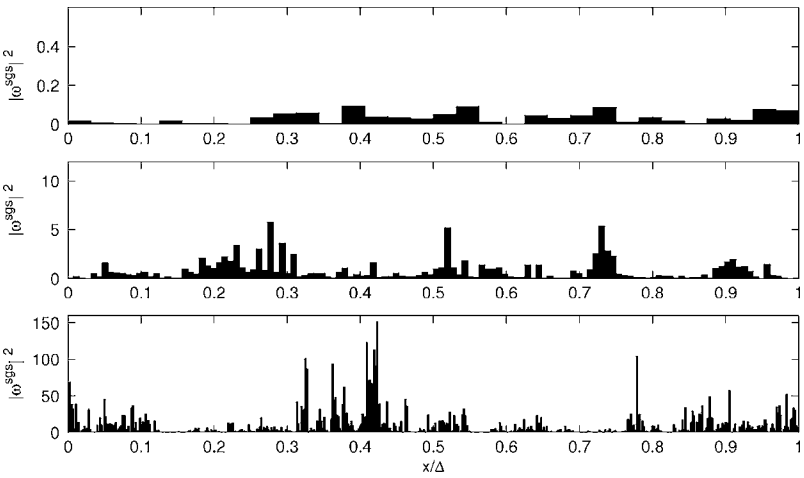

FIG. 2. Effect of increasing Re_Δ on the enstrophy cascade, showing enstrophy fields $|\boldsymbol{\omega}^{sgs}(\mathbf{x},t)|^2$ at three successively higher Re_Δ values (top to bottom) for the same total subgrid enstrophy Q_{sgs}; note reduction in inner scale λ_ν and increasing intermittency as Re_Δ increases.

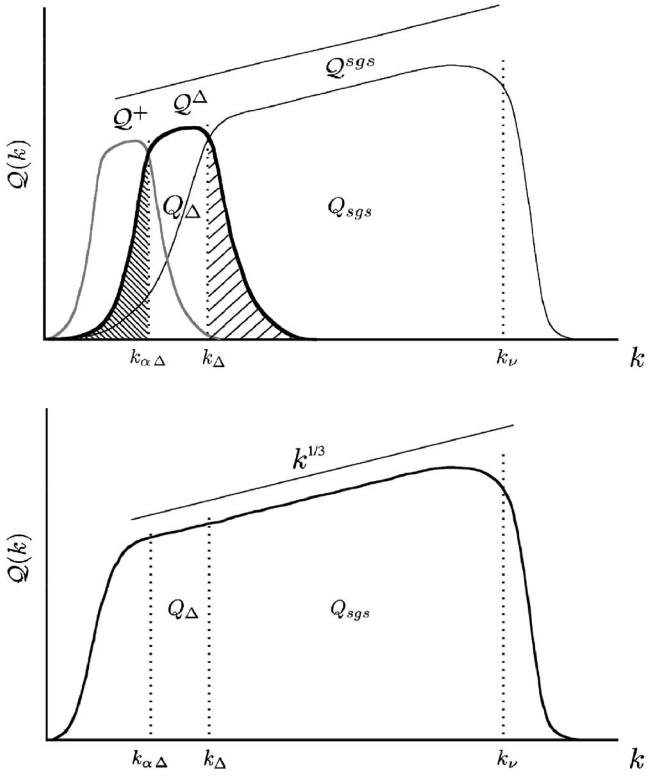

FIG. 3. Log-log schematic showing (top) enstrophy spectrum composed of subgrid part, Δ-scale part, and contribution from remainder of resolved-scale vorticity field, and (bottom) inertial-range scaling used to determine total subgrid enstrophy Q_{sgs} between scales Δ and λ_ν from enstrophy Q_Δ in resolved field between scales Δ and $\alpha\Delta$.

subgrid enstrophy field on the filter scale Δ at three successively higher Re_Δ values. The reduction in inner-scale cell size λ_ν with increasing Re_Δ, as well as the increasing intermittency in the subgrid enstrophy as the number $\mathcal{N}$ of cascade steps increases with Re_Δ, is readily apparent. Both of these characteristics result naturally from the multifractal cascade in (9).

With the subgrid vorticity $\boldsymbol{\omega}^{sgs}$ modeled throughout each resolved-scale grid cell in this manner, the subgrid velocity components u_i^{sgs} appearing in τ_{ij}^* are then obtained from Biot–Savart integrals over the subgrid-vorticity field in (7). The resulting subgrid velocity components u_i^{sgs} are then used to directly formulate τ_{ij}^* via (5).

A. The vorticity magnitude cascade

Specifying the vorticity magnitude in each inner-scale cell first requires determining the total subgrid enstrophy that the multiplicative cascade must distribute within each LES grid cell in terms of the average subgrid enstrophy Q_{sgs} over the grid cell. This can be obtained from classical equilibrium inertial-range scaling arguments when the grid scale Δ lies in the inertial range, as indicated in Fig. 3.

To find the average subgrid enstrophy Q_{sgs}, we first determine the average enstrophy Q_Δ in the resolved field between the filter scale Δ and any larger inertial-range scale $\alpha\Delta$. This is obtained from the contribution u_i^Δ to the resolved velocity from this scale range, namely

$$u_i^\Delta \equiv \bar{u}_i - (\bar{u}_i)_{\alpha\Delta}, \tag{11}$$

where $(\bar{u}_i)_{\alpha\Delta}$ denotes the velocity obtained by filtering the resolved field $\bar{u}_i$ at scale $\alpha\Delta$. The curl of $\mathbf{u}^\Delta$ then gives the resolved vorticity $\boldsymbol{\omega}^\Delta$ associated with this same scale range, from which the corresponding enstrophy $Q_\Delta \equiv \omega_i^\Delta \omega_i^\Delta$ may be defined. The vorticity field therefore consists of the sum of the subgrid part $\boldsymbol{\omega}^{sgs}$, the Δ-scale part $\boldsymbol{\omega}^\Delta$, and the remainder of the resolved field $\boldsymbol{\omega}^+$. The enstrophy field $Q \equiv \omega_i \omega_i$ thus is the sum of the three square terms resulting from the subgrid part $Q_{sgs} \equiv \omega_i^{sgs} \omega_i^{sgs}$, the Δ-scale part $Q_\Delta \equiv \omega_i^\Delta \omega_i^\Delta$, and the remainder $Q_+ \equiv \omega_i^+ \omega_i^+$, and the three cross terms $2(\omega_i^{sgs}\omega_i^\Delta)$, $2(\omega_i^{sgs}\omega_i^+)$ and $2(\omega_i^+\omega_i^\Delta)$. Averages over the cross terms will be small, since widely disparate scale ranges in the vorticity field are essentially uncorrelated.

The total enstrophy field is thus $Q \approx Q_{sgs} + Q_\Delta + Q_+$, and its spectrum $\mathcal{Q}(k)$ is thus the sum of $\mathcal{Q}_{sgs}$, $\mathcal{Q}_\Delta$, and $\mathcal{Q}_+$, as indicated in Fig. 3(a). The tails of each part on either side of k_Δ and $k_{\alpha\Delta}$ result from the nonlinear nature of the enstrophy, even for spectrally sharp filtering of the velocity field. However, owing to the near symmetry of these tails as indicated in Fig. 3(a), for sufficiently small α the area under $\mathcal{Q}(k)$ between k_Δ and $k_{\alpha\Delta}$ approaches the total area Q_Δ over all k. As a result, the enstrophy Q_Δ allows determination of Q_{sgs} as indicated in Fig. 3(b) by integrating the enstrophy spectrum $\mathcal{Q}(k)$ from the filter-scale wave number k_Δ to the inner-scale wave number k_ν. On dimensional grounds, the enstrophy spectrum $\mathcal{Q}(k)$ in the inertial range scales with the wave number k and mean dissipation rate ε as $\mathcal{Q}(k) \sim \varepsilon^{2/3} k^{1/3}$, giving

$$Q_{sgs} = \int_{k_\Delta}^{k_\nu} \mathcal{Q}(k)dk = \kappa\, Q_\Delta \left[\left(\frac{k_\nu}{k_\Delta} \right)^{4/3} - 1 \right], \tag{12}$$

where

$$\kappa \equiv (1 - \alpha^{-4/3})^{-1}. \tag{13}$$

For $\alpha = 2$ as will be used in Secs. IV and V, $\kappa \approx 1.66$.

The subgrid enstrophy Q_{sgs} in (12) is distributed over each grid-scale cell by a three-dimensional stochastic multiplicative cascade to give the subgrid vorticity magnitude in each inner-scale cell as

$$|\boldsymbol{\omega}^{sgs}|(\mathbf{x},t) = \left[Q_{sgs}(2^{\mathcal{N}})^3 \prod_{n=1}^{\mathcal{N}} \mathcal{M}_n(\mathbf{x},t) \right]^{1/2}, \tag{14}$$

where $\mathcal{N}$ from (10) is the number of cascade steps, and the multipliers $\mathcal{M}_n$ correspond to random samples from the scale-invariant distribution $P(\mathcal{M})$ for the enstrophy field (e.g., Refs. 44 and 45). This leads naturally to a multifractal subgrid enstrophy field.

B. The vorticity orientation cascade

Experimental and computational evidence[14,15,20,46] indicates that the orientations of the subgrid velocity field are highly correlated with the $\mathbf{u}^\Delta$ orientations. The present model builds on these results in deriving the orientation cascade. Specifically, the orientations in the subgrid vorticity field $\boldsymbol{\omega}^{sgs}$ are taken to decorrelate at successively smaller scales from the local orientation of $\boldsymbol{\omega}^\Delta$ at the smallest resolved

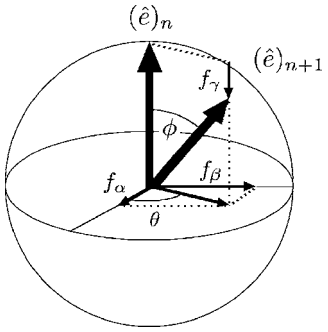

FIG. 4. Spherical angles (θ,ϕ) and unit-vector increments $(\delta_i,\delta_j,\delta_k)$ describing decorrelation of vorticity orientation $(\hat{\mathbf{e}})_{n+1}$ at stage $(n+1)$ from $(\hat{\mathbf{e}})_n$ at stage (n).

scale, here denoted by the unit vector $\hat{\mathbf{e}}^\Delta(\mathbf{x},t)$. Between any two successive stages (n) and $(n+1)$ in the cascade, the corresponding vorticity orientations $(\hat{\mathbf{e}})_{n+1}$ and $(\hat{\mathbf{e}})_n$ thus deviate by stochastic spherical decorrelation angles θ and ϕ, as indicated in Fig. 4. Each component of the orientation unit-vector at stage $(n+1)$ is therefore determined as

$$(\hat{e}_i)_{n+1} = (\hat{e}_i)_n + f_i(\phi,\theta)_{n+1}, \tag{15}$$

where $f_\alpha(\phi,\theta)=\sin\phi\cos\theta$, $f_\beta(\phi,\theta)=\sin\phi\sin\theta$ and $f_\gamma(\phi,\theta)=\cos\phi-1$.

The local strain rate tensor in the resolved scales can be expected to influence the local distribution of angles in at least the first few steps of the orientation cascade. With the framework of the present modeling approach, this would manifest itself in the form of correlations between the angle distribution and the multiplier values $\mathcal{M}$. In particular, while the distribution in Fig. 4 would be expected to be uniform, the ϕ distribution would be strongly correlated with the multiplier values $\mathcal{M}$. This can be seen in the conditional probability distributions $P(\cos\phi;\mathcal{M})$ shown in Fig. 5, obtained from present analyses of DNS data. It is apparent that at low multiplier values $\mathcal{M}$ there is only a weak correlation between vorticity orientations at two successive scales in the cascade, while at large multiplier values the corresponding unit vectors $(\hat{\mathbf{e}})_n$ and $(\hat{\mathbf{e}})_{n+1}$ become nearly identical, since $\cos\phi\to 1$. This is consistent with the observed tendency of the strongest vortical structures, which correspond to high multiplier values, to maintain a preferred alignment with the local strain rate tensor over a relatively large range of length scales.

Based on the above considerations, the intermittency factor $\mathcal{I}$ can be defined from a correlation between $\boldsymbol{\omega}^{sgs}$ and $\boldsymbol{\omega}^\Delta$ as

$$\mathcal{I} = \int_{\mathbf{x}'} \boldsymbol{\omega}^{sgs}\cdot\boldsymbol{\omega}^\Delta d^3\mathbf{x}' \Bigg/ \int_{\mathbf{x}'} |\boldsymbol{\omega}^{sgs}||\boldsymbol{\omega}^\Delta| d^3\mathbf{x}'. \tag{16}$$

The subgrid vorticity field $\boldsymbol{\omega}^{sgs}$ after $\mathcal{N}$ cascade steps can then be expressed in terms of $\mathcal{I}(\mathcal{N})$ as

$$\boldsymbol{\omega}^{sgs}(\mathbf{x},t) = |\boldsymbol{\omega}^{sgs}|\left(\mathcal{I}(\mathcal{N})\hat{\mathbf{e}}^\Delta(\mathbf{x},t) + (1-\mathcal{I})\sum_{n=1}^{\mathcal{N}}\boldsymbol{\delta}_n\right), \tag{17}$$

where $\boldsymbol{\delta}_n$ are the decorrelation increments in the orientation cascade. Owing to the stochastic nature of both the multiplier values $\mathcal{M}_n$ in the magnitude cascade and the decorrelation increments $\boldsymbol{\delta}_n$ in the orientation cascade, the subgrid vorticity $\boldsymbol{\omega}^{sgs}(\mathbf{x},t)$ is a stochastic field. From (17) its expectation value $\langle\boldsymbol{\omega}^{sgs}\rangle$ involves correlations between the multipliers $\mathcal{M}_n$ and the increments $\boldsymbol{\delta}_n$. In principle, the effect of these correlations could be incorporated within the framework of the present model, in a somewhat similar spirit as the various approaches for conditional averaging done in "optimal LES" of Langford and Moser.[47] If, however, the net effect of the correlations on the expectation value of the subgrid vorticity is taken to be sufficiently weak, then

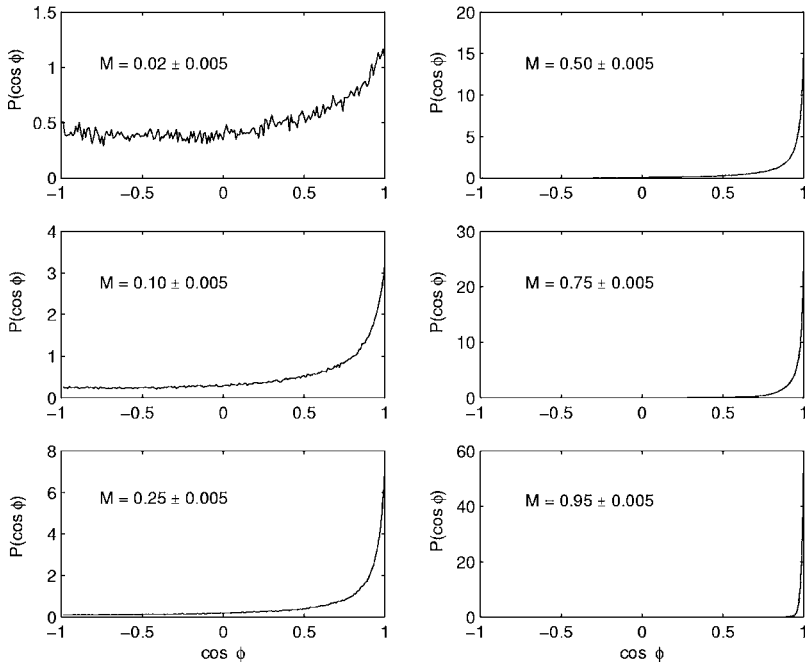

FIG. 5. Probability distribution of decorrelation angle ϕ in Fig. 4, conditioned on multiplier values $\mathcal{M}$ from the DNS data and showing strong correlation in alignment between successive stages in cascade when $\mathcal{M}$ is large.

$$\langle \boldsymbol{\omega}^{sgs} \rangle = \mathcal{I}(\mathcal{N}) \langle |\boldsymbol{\omega}^{sgs}| \rangle \hat{\mathbf{e}}^{\Delta} + (1 - \mathcal{I}) \langle |\boldsymbol{\omega}^{sgs}| \rangle \sum_{n=1}^{\mathcal{N}} \langle \boldsymbol{\delta}_n \rangle. \tag{18}$$

Furthermore, if as noted above the decorrelation cascade is taken to be fully isotropic, then the expectation value of the increments in (18) vanishes, giving from (14)

$$\langle \boldsymbol{\omega}^{sgs} \rangle = \mathcal{I}(\mathcal{N}) (2^{\mathcal{N}})^{3/2} \langle (\mathcal{M}_1 \cdots \mathcal{M}_{\mathcal{N}})^{1/2} \rangle Q_{sgs}^{1/2} \hat{\mathbf{e}}^{\Delta}, \tag{19}$$

where Q_{sgs} comes from (12). While the correlations between the multipliers and the angles in the orientation cascade have in (19) been taken to be negligible, the results in Sec. V and in Part II (Ref. 34) will show that the effect of this appears to be comparatively small.

C. Biot–Savart evaluation of the subgrid velocities

The expectation value of the subgrid velocities $\langle \mathbf{u}^{sgs} \rangle$ is obtained from the corresponding subgrid vorticity $\langle \boldsymbol{\omega}^{sgs} \rangle$ in (19) via the Biot–Savart integral in (7) as

$$\langle \mathbf{u}^{sgs} \rangle \equiv \frac{1}{4\pi} \int_{\mathbf{x}'} \langle \boldsymbol{\omega}^{sgs} \rangle \times \mathbf{K} \, d^3\mathbf{x}'. \tag{20}$$

Since the distribution $P(\mathcal{M})$ of the multipliers in $\langle \boldsymbol{\omega}^{sgs} \rangle$ is the same everywhere, from (19) and (20) the expectation value becomes

$$\langle \mathbf{u}^{sgs} \rangle = \mathcal{I}(\mathcal{N}) (2^{\mathcal{N}})^{3/2} \langle (\mathcal{M}_1 \cdots \mathcal{M}_{\mathcal{N}})^{1/2} \rangle \times \left(\frac{Q_{sgs}}{Q_{\Delta}} \right)^{1/2} \frac{1}{4\pi} \int_{\mathbf{x}'} Q_{\Delta}^{1/2} \hat{\mathbf{e}}^{\Delta} \times \mathbf{K} \, d^3\mathbf{x}'. \tag{21}$$

The Biot–Savart integral in (21) is simply $\mathbf{u}^{\Delta}$, giving with (10) and (12)

$$\langle \mathbf{u}^{sgs} \rangle = \mathcal{I}(\mathcal{N}) 2^{3/2\mathcal{N}} \langle \mathcal{M}^{1/2} \rangle^{\mathcal{N}} [2^{4/3\mathcal{N}} - 1]^{1/2} \sqrt{\kappa} \, \mathbf{u}^{\Delta}, \tag{22}$$

where we have also made use of the fact that the multipliers are statistically independent.

D. The subgrid stress tensor τ_{ij}^{*}

From (22) the subgrid velocity component values u_i^{sgs} can be written as

$$u_i^{sgs}(\mathbf{x},t) \approx \mathcal{I}(\mathcal{N}) \mathcal{A}(\mathcal{N}) \sqrt{\kappa} u_i^{\Delta}(\mathbf{x},t), \tag{23}$$

where

$$\mathcal{A} \equiv 2^{(3/2)\mathcal{N}} \langle \mathcal{M}^{1/2} \rangle^{\mathcal{N}} [2^{(4/3)\mathcal{N}} - 1]^{1/2}. \tag{24}$$

The intermittency factor $\mathcal{I}$ from (16) that appears in (23) is implied by the required Re_{Δ} independence of u_i^{sgs} as $Re_{\Delta} \to \infty$. As correspondingly $\mathcal{N} \to \infty$ this requires

$$\mathcal{I}(\mathcal{N}) \approx C_{\mathcal{I}} 2^{-(2/3+3/2)\mathcal{N}} \langle \mathcal{M}^{1/2} \rangle^{-\mathcal{N}}. \tag{25}$$

The associated proportionality constant $C_{\mathcal{I}}$ should be universal, and can be obtained from *a priori* testing as done in Sec. V, with the result that $C_{\mathcal{I}} \approx 0.37$. This gives the subgrid stress τ_{ij}^{*} as

$$\tau_{ij}^{*} \approx \mathcal{B}(\overline{\bar{u}_i u_j^{\Delta}} + \overline{\bar{u}_j u_i^{\Delta}}) + \mathcal{B}^2 \overline{u_i^{\Delta} u_j^{\Delta}}, \tag{26}$$

where

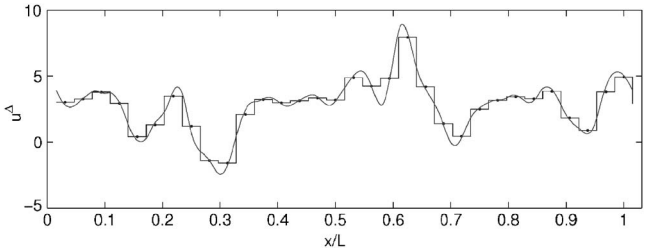

FIG. 6. Schematic representation of Legendre interpolation in (28) and (30) of continuous resolved velocity fields $\bar{u}_i(\mathbf{x})$ and $u_i^{\Delta}(\mathbf{x})$ from cell-centered values on resolved grid, used to evaluate filtered product terms (31) and (32) appearing in subgrid stress τ_{ij}^{*} in (26).

$$\mathcal{B} \equiv 0.47 \, 2^{-(2/3)\mathcal{N}} [2^{(4/3)\mathcal{N}} - 1]^{1/2}, \tag{27}$$

and where $\mathcal{N}$ is from (10) and u_i^{Δ} is from (11). This involves only quantities available from the resolved scales of the flow, thus closing the subgrid-stress term in the momentum equation in (6).

IV. EXPLICIT FILTERING IN τ_{ij}^{*} AND $\overline{\bar{u}_i \bar{u}_j}$

Each of the terms in (26) as well as the nonlinear inertial term in (6) involves an explicit filter at scale Δ, denoted by the long overbar. As regards the inertial term, previous studies[30,48,49] have shown that the choice of explicit filter affects both the resolved velocity field and the implied subgrid energy transfer field. Here this filter is taken as an explicit three-dimensional Legendre box average over each grid-scale cell. Note that the fields $\bar{\mathbf{u}}$ and $\mathbf{u}^{\Delta}$ in these filtered product terms vary continuously over each grid cell. Thus the component fields $\bar{u}_i(\mathbf{x})$ and $u_i^{\Delta}(\mathbf{x})$ that must be filtered over each grid cell are approximated by second-order three-dimensional Legendre expansions of the form

$$\bar{u}_i(\mathbf{x}) \approx \sum_{l,m,n} a_{lmn} \Phi_l(x) \Phi_m(y) \Phi_n(z) \equiv \mathcal{G}_i(\mathbf{x}), \tag{28}$$

where Φ_k are the Legendre basis functions in each of the three coordinate directions. The second-order Legendre basis is compact, since it uses only the 26 immediately adjacent grid-cell values, is well-conditioned, and exactly recovers the original cell-centered field values, as indicated in Fig. 6. Moreover as indicated in Fig. 7, for $\alpha = 2$ the resulting $(\bar{u}_i)_{2\Delta}$ in (11) at the cell center is simply the resolved velocity field in (28) filtered over the cubic volume $(2\Delta)^3$. This corresponds in the mapped Legendre coordinates to a filter over the entire cubic Legendre interval. Thus $(\bar{u}_i)_{2\Delta}$ has already been evaluated as the coefficient a_{000} in the Legendre expansion of $\bar{u}_i$ in (28), thereby allowing rapid calculation of the cell-centered velocities u_i^{Δ} in (11) as

$$u_i^{\Delta} \equiv \bar{u}_i - a_{000}. \tag{29}$$

From (29) the resulting cell-centered u_i^{Δ} values give the corresponding Legendre expansion for the continuous component fields $u_i^{\Delta}(\mathbf{x})$ throughout each grid cell as

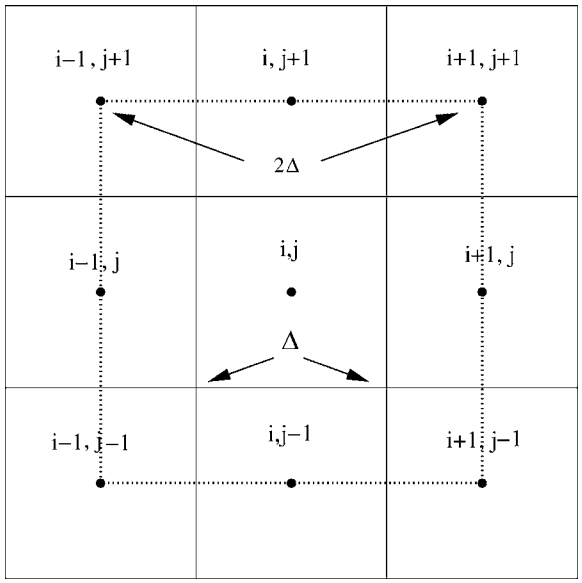

FIG. 7. Two-dimensional schematic indicating local Legendre interpolation of $\bar{u}_i$ in given grid cell at scale Δ; when mapped into canonical Legendre interval the coefficient a_{000} from (28) is equivalent to $(\bar{u}_i)_{2\Delta}$ needed to evaluate $\mathbf{u}^{\Delta}$ in (11), as indicated in (29).

$$u_i^{\Delta}(\mathbf{x}) \approx \sum_{l,m,n} b_{lmn}\Phi_l(x)\Phi_m(y)\Phi_n(z) \equiv \mathcal{H}_i(\mathbf{x}). \tag{30}$$

The filtered products in the subgrid stress τ_{ij}^* in (26) are then explicitly evaluated by integrating over the grid-cell volume as

$$\overline{\bar{u}_i u_j^{\Delta}} \approx \frac{1}{\Delta^3}\int_{\Delta^3} \mathcal{G}_i(\mathbf{x})\mathcal{H}_j(\mathbf{x})d^3\mathbf{x}, \tag{31}$$

$$\overline{u_i^{\Delta} u_j^{\Delta}} \approx \frac{1}{\Delta^3}\int_{\Delta^3} \mathcal{H}_i(\mathbf{x})\mathcal{H}_j(\mathbf{x})d^3\mathbf{x}, \tag{32}$$

and similarly the explicit filter on the inertial term in (6) is evaluated as

$$\overline{\bar{u}_i \bar{u}_j} \approx \frac{1}{\Delta^3}\int_{\Delta^3} \mathcal{G}_i(\mathbf{x})\mathcal{G}_j(\mathbf{x})d^3\mathbf{x}. \tag{33}$$

Equations (26)–(33) allow evaluation of the deviatoric part of τ_{ij}^* and the nonlinear term $\overline{\bar{u}_i\bar{u}_j}$ in (6), and together provide a complete statement of the multifractal subgrid-scale model for large-eddy simulation.

V. *A PRIORI* TESTS OF THE MULTIFRACTAL MODEL

The accuracy of the multifractal model for the subgrid-scale stresses τ_{ij}^* can be assessed in *a priori* tests using filtered DNS data to simulate the resolved scales of a large-eddy simulation, and comparing quantities obtained from the model with corresponding quantities obtained from the subgrid scales in the DNS data. While there are known limitations inherent in comparisons of modeling approaches against DNS data, such testing provides valuable information about subgrid model accuracy, especially for structural models like the present, which recover the actual instantaneous structure of the subgrid field. High-fidelity recovery of the subgrid field should correlate with reduced dynamical error in the deterministic evolution of the resolved scales, as discussed in the "ideal LES" formalism of Langford and Moser.[47] This, in turn, should correlate with higher-fidelity recovery of the resolved scales in an actual LES calculation.

Such assessments are here based on a 512^3 direct numerical simulation of forced, homogeneous, isotropic turbulence in a cubic, periodic domain at $Re_\lambda \approx 170$ by Jimenez *et al.*[50] The filtered velocity fields were obtained from the DNS data by spatial averaging using three-dimensional box filters of size $\Delta = m\delta x$, where m sets the filter scale, and $\delta x \equiv L/512$ with L the length scale of the computational domain. Tests were conducted with $m=16$ corresponding to resolved-scale Reynolds number $Re_\Delta \approx 160$, and with $m=128$ corresponding to $Re_\Delta \approx 2550$. The smaller of these filter scales is in the range where multifractal scaling has been verified[44] in the subgrid enstrophy field, while the larger lies outside this range and thereby provides an indirect test of the robustness of the model.

A. The filtered subgrid velocities $\overline{u_i^{sgs}}$

The filtered velocity fields $\bar{u}_i$ supplied to the subgrid-scale model were first used to construct the subgrid velocity field from (11) and (23), and the resulting fields then filtered at the scale Δ using the explicit Legendre box filter to give the filtered subgrid velocity component fields $\overline{u_i^{sgs}}$. Typical one-dimensional intersections through these fields for the $Re_\Delta \approx 160$ case, for which there are 32 points defining the fields in each intersection, are shown by the dashed lines and crosses in Fig. 8. These model results were then compared with the filtered residual velocity fields obtained by subtracting the filtered velocity fields $\bar{u}_i$ from the original DNS velocities and applying the Legendre box filter at the same scale Δ. Corresponding intersections through these fields are also shown by the solid lines for comparison. If the subgrid model were ideal, these fields would be identical, and it is apparent that there is overall good agreement between them. In general the model accurately captures both the magnitude of the local filtered subgrid velocity field and its orientation, with the latter being evident from the fact that generally all three component fields simultaneously agree well with the residual fields from the DNS data.

In the $Re_\Delta \approx 2550$ case there are only four points in these filtered fields in each coordinate direction, so one-dimensional intersections of the type in Fig. 8 provide little indication of the structure in these fields. However, correlations between the filtered subgrid velocity component fields from the multifractal model and from the DNS data can be readily computed for both the $Re_\Delta \approx 160$ and $Re_\Delta \approx 2550$ cases, and are shown in Fig. 9. The model is seen to produce correlations exceeding 0.91 at the lower Re_Δ, and slightly higher values at the larger Re_Δ, indicating good agreement between the model and DNS values. In all of these results, $C_{\mathcal{I}}$ from (25) has been set to optimize the agreement at both $Re_\Delta \approx 160$ and $Re_\Delta \approx 2550$, giving the value $C_{\mathcal{I}} \approx 0.37$.

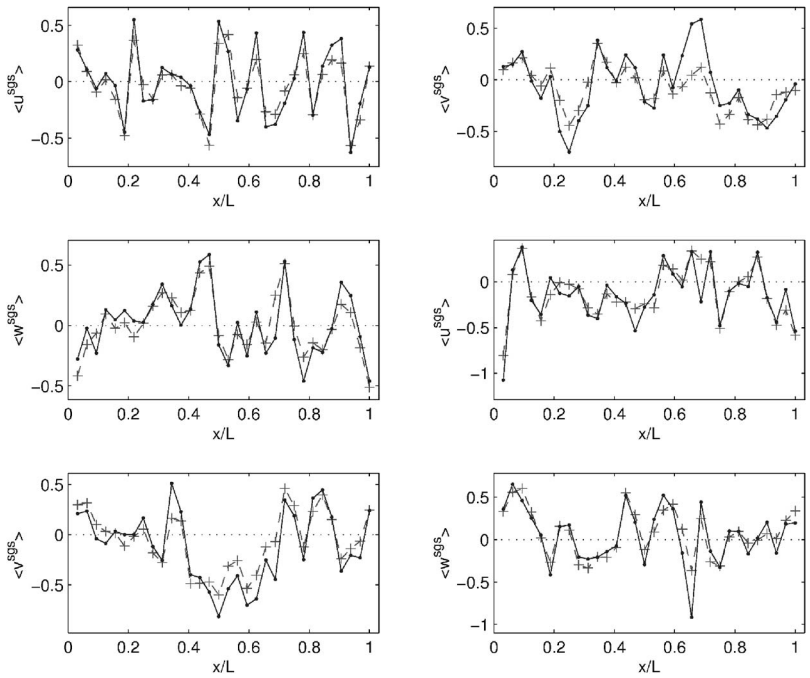

FIG. 8. Typical one-dimensional intersections through filtered subgrid velocity component fields $\overline{u_i^{sgs}}(\mathbf{x},t)$ from *a priori* tests of (23) at $Re_\Delta \approx 160$, comparing DNS (solid) and model (dashed with crosses) fields and showing good agreement of results from present multifractal model; correlation coefficient between DNS and model values exceeds 0.91.

B. The subgrid stress tensor τ_{ij}^*

The subgrid stress tensor component fields τ_{ij}^* implied by the multifractal model were evaluated from (26) and compared with the corresponding fields obtained from the DNS data via (5). Typical 32-point intersections through all six of these component fields for the $Re_\Delta \approx 160$ case are shown in Fig. 10, with dashed lines with crosses and solid lines again giving results from the model and the DNS data, respectively. Generally good magnitude and phase agreement is seen between the modeled and actual values, indicating relatively accurate representation of momentum exchange between the resolved and subgrid scales in the multifractal subgrid model.

Figures 11 and 12 show the resulting correlations between results from the multifractal model and from the DNS data for, respectively, the normal and shear components of the subgrid stress fields. For the normal stress component fields in Fig. 11, the resulting correlation coefficients are

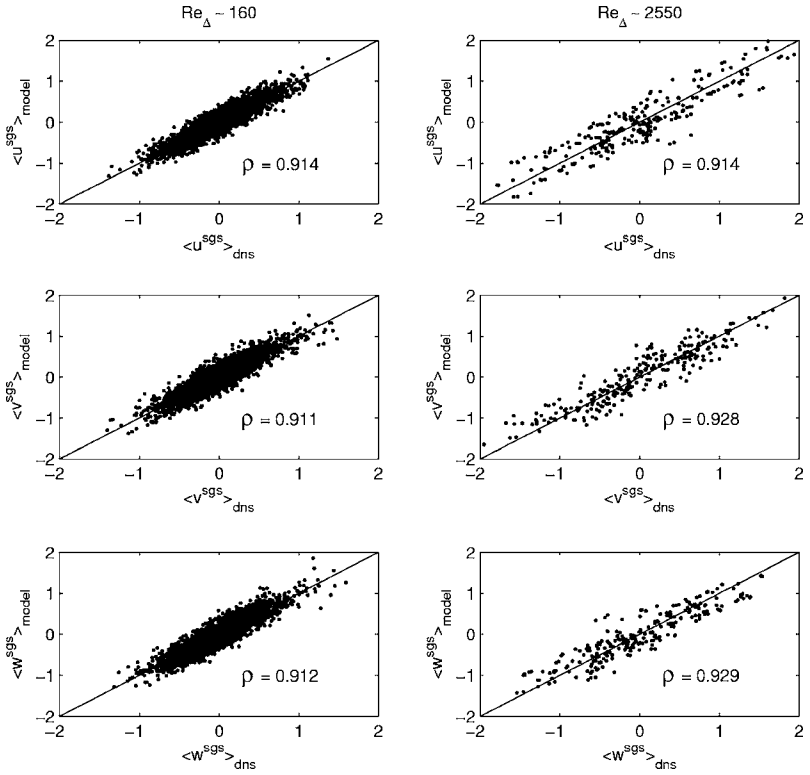

FIG. 9. Correlations between DNS and model values for filtered subgrid velocity component fields $\overline{u_i^{sgs}}(\mathbf{x},t)$ from *a priori* testing of (23) at $Re_\Delta \approx 160$ (left) and $Re_\Delta \approx 2550$ (right), yielding correlation coefficients exceeding 0.91 at both Re_Δ values.

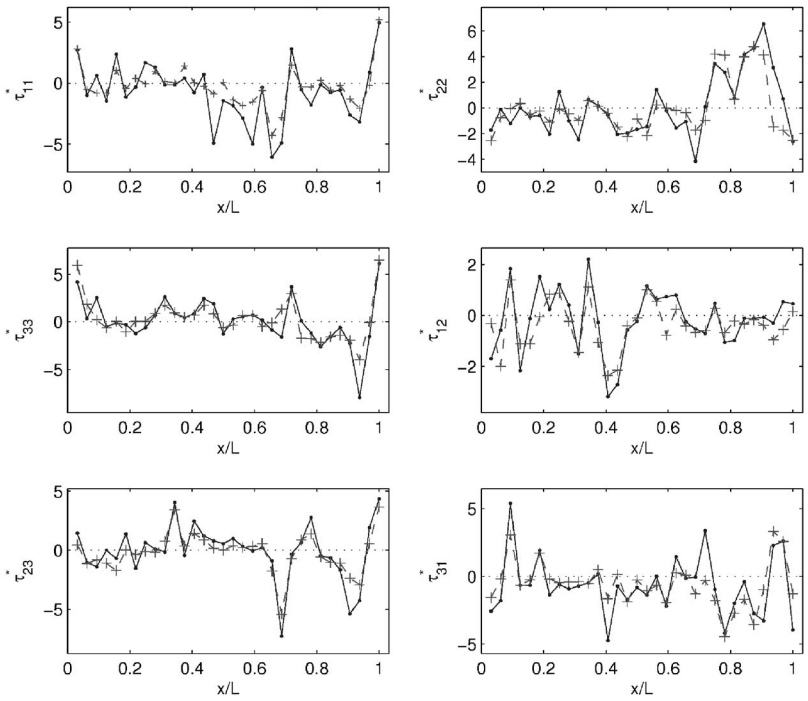

FIG. 10. Typical one-dimensional intersections through subgrid stress component fields $\tau^*_{ij}(\mathbf{x},t)$ from *a priori* tests of (26) at $Re_\Delta \approx 160$, comparing DNS (solid) and model (dashed with crosses) fields and showing generally good agreement of results from present multifractal model; correlation coefficient between DNS and model values is 0.86.

about 0.86 in the $Re_\Delta \approx 160$ case, and range from 0.65–0.80 in the $Re_\Delta \approx 2550$ case. For the shear stress component fields in Fig. 12, the correlation coefficients are again about 0.86 in the $Re_\Delta \approx 160$ case, and range from 0.57–0.70 in the $Re_\Delta \approx 2550$ case.

The origin of the lower correlations for the subgrid stress component fields noted above can be traced to the correlations between subgrid velocity components that have, for the present, been neglected in evaluating the Biot–Savart integrals. This can be seen in Fig. 13, which shows typical 32-point one-dimensional intersections for the individual terms in the decomposition of τ^*_{ij} for the $Re_\Delta \approx 160$ case, with dashed lines with crosses and solid lines again giving the model and DNS results, respectively. Note that the two "resolved-subgrid" interaction terms in (5) are relatively accurately represented by the model, but the "subgrid-subgrid" term is essentially zero. Corresponding correlations between model and DNS results for each of these fields are shown in Fig. 14 for both the $Re_\Delta \approx 160$ and 2550 cases. Correlation coefficients for the "resolved-subgrid" interaction terms are

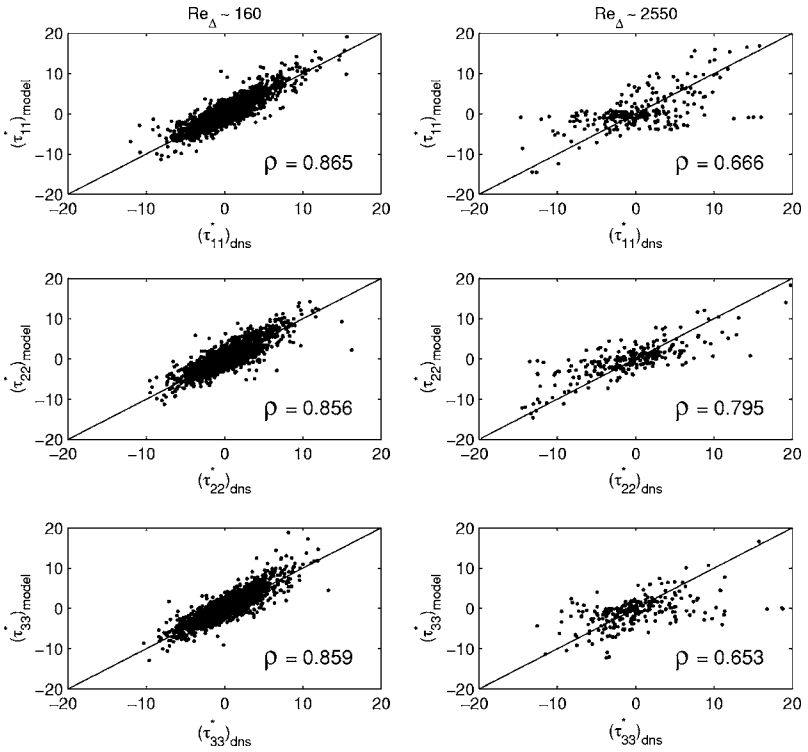

FIG. 11. Correlations between DNS and model values for normal components of subgrid stress fields $\tau^*_{ij}(\mathbf{x},t)$ from *a priori* testing of (26) at $Re_\Delta \approx 160$ (left) and $Re_\Delta \approx 2550$ (right), yielding correlation coefficients as shown.

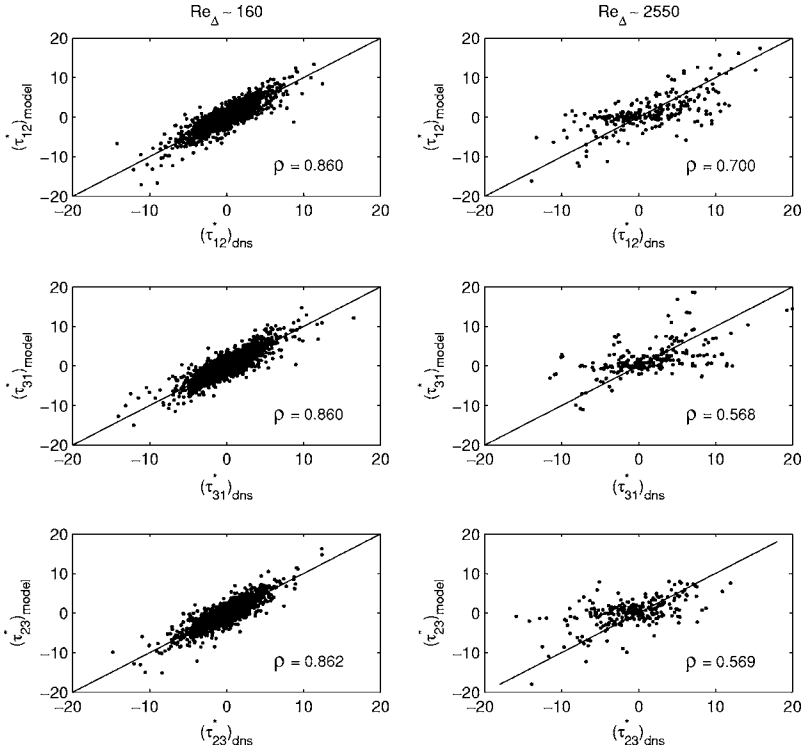

FIG. 12. Correlations between DNS and model values for shear components of subgrid stress fields $\tau_{ij}^{*}(\mathbf{x},t)$ from *a priori* testing of (26) at $Re_\Delta \approx 160$ (left) and $Re_\Delta \approx 2550$ (right), yielding correlation coefficients as shown.

about 0.88 at the lower Re_Δ and 0.75 at the higher Re_Δ. For the "subgrid-subgrid" term, the correlation coefficients are only 0.38 and 0.32 at the lower and higher Re_Δ values. Note that it may be possible to incorporate correlations between subgrid velocity component fields in evaluation of the Biot–Savart integrals in Sec. III C and thereby better model the "subgrid-subgrid" term in (26), however, in the results presented here these correlations are being neglected entirely.

C. The subgrid energy production field

As noted in the Introduction, while errors in representing the subgrid stresses in large-eddy simulations will introduce inaccuracies in momentum transport in the flow, simulations typically seek at a minimum to transport kinetic energy between the resolved and subgrid scales with reasonable accuracy. Accordingly, Fig. 15 shows six typical one-dimensional

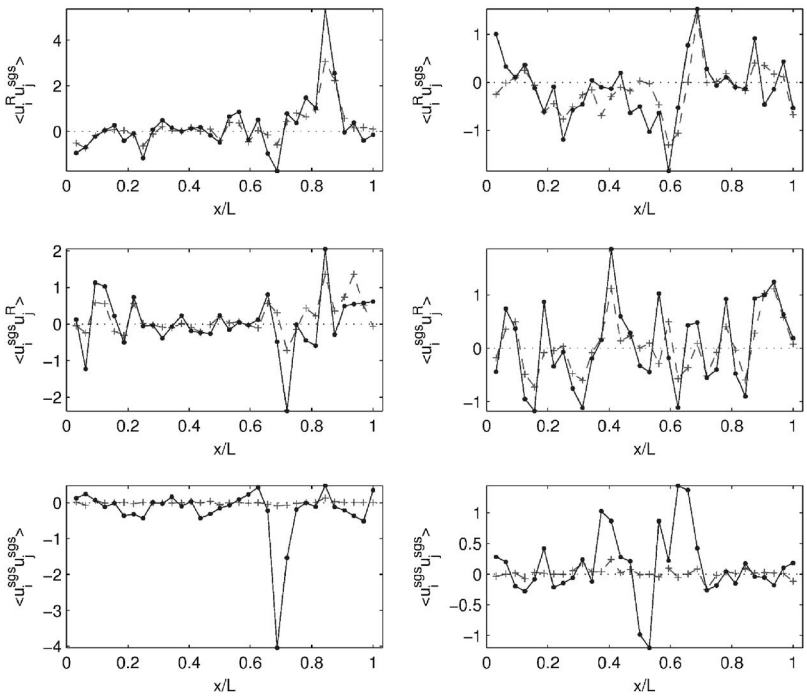

FIG. 13. Typical one-dimensional intersections through "resolved-subgrid" interaction fields $\overline{u_i^R u_j^{sgs}}(\mathbf{x},t)$ (top and middle rows) and "subgrid-subgrid" interaction fields $\overline{u_i^{sgs} u_j^{sgs}}(\mathbf{x},t)$ (bottom row) from *a priori* tests of (26) at $Re_\Delta \approx 160$, comparing DNS values (solid) and model values (dashed with crosses). Note that subgrid-subgrid interaction is not well accounted for in model due to present neglect of correlations in cascade.

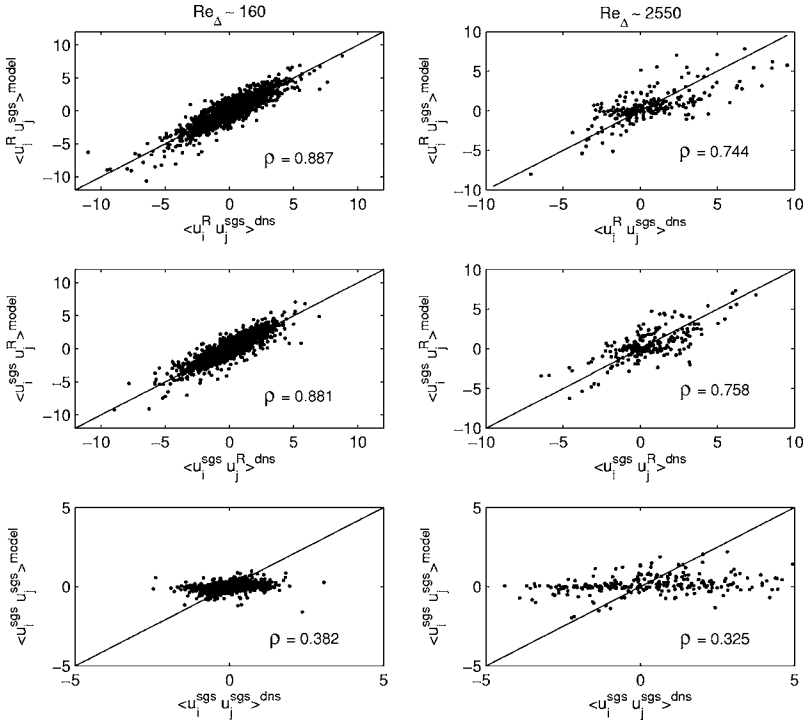

FIG. 14. Correlations between DNS and model values for "resolved-subgrid" interaction fields $\overline{u_i^R u_j^{sgs}}(\mathbf{x},t)$ (top and middle rows) and "subgrid-subgrid" interaction fields $u_i^{sgs}u_j^{sgs}(\mathbf{x},t)$ (bottom row) obtained from *a priori* testing of (26) at $Re_\Delta \approx 160$ (left) and $Re_\Delta \approx 2550$ (right), yielding correlation coefficients as shown.

intersections through the subgrid energy production field $\mathcal{P}^*(\mathbf{x},t) \equiv -\tau_{ij}^* \bar{S}_{ij}$ obtained from the subgrid stress tensor field $\tau_{ij}^*(\mathbf{x},t)$ for the $Re_\Delta \approx 160$ case, with dashed lines with crosses and solid lines giving results from the model and the DNS data, respectively. It is apparent that, despite the errors noted above in the "subgrid-subgrid" term of the stress tensor τ_{ij}^*, the subgrid energy production field is relatively well reproduced by the model, including both the forward and backscatter of energy from the resolved scales. Figure 16 shows the correlations between subgrid energy production fields from the multifractal model and from the DNS data for both the $Re_\Delta \approx 160$ and 2550 cases. The resulting correlation coefficients are 0.85 in the $Re_\Delta \approx 160$ case, and 0.61 in the $Re_\Delta \approx 2550$ case.

D. Analysis of model errors

Previous studies[51–55] have examined the effect of numerical errors on the performance of subgrid models. Ghosal[51] in particular has examined these errors in the context of large-eddy simulations with the dynamic Smagorinsky model, in which the constant C_s is locally determined

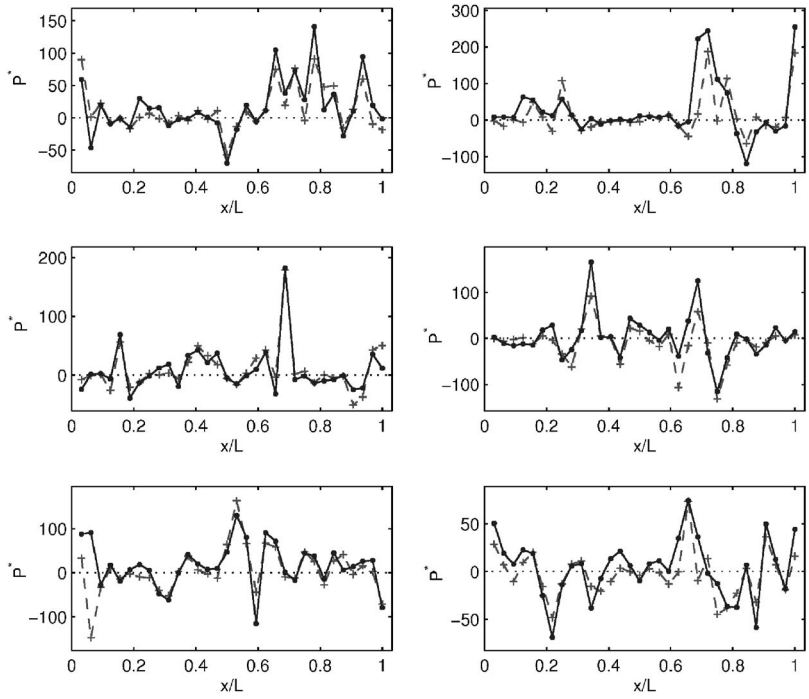

FIG. 15. Typical one-dimensional intersections through subgrid energy production field $\mathcal{P}^*(\mathbf{x},t)$ from *a priori* tests of (26) at $Re_\Delta \approx 160$, comparing DNS (solid) and model (dashed with crosses) fields and showing generally good agreement of both forward ($\mathcal{P}^* < 0$) and backward ($\mathcal{P}^* > 0$) transfer of energy between resolved and subgrid scales.

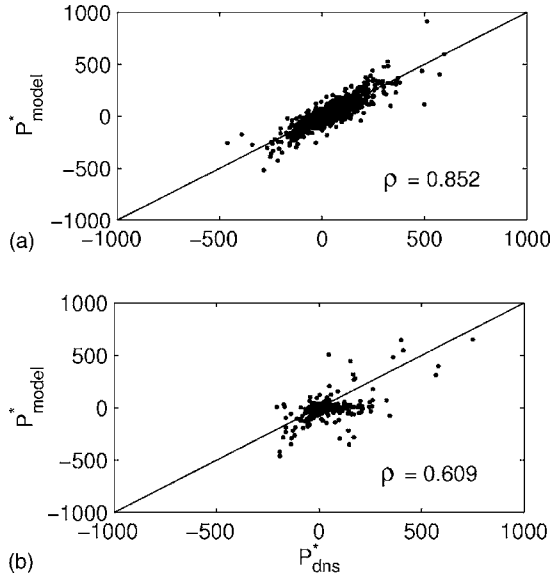

FIG. 16. Correlations between DNS and model values for subgrid energy production fields $\mathcal{P}^*(\mathbf{x},t)$ from *a priori* testing of (26) at $Re_\Delta \approx 160$ (top) and $Re_\Delta \approx 2550$ (bottom), yielding correlation coefficients as shown. Accounting for subgrid-subgrid interactions in Figs. 13 and 14 due to correlations in the cascade, which are presently neglected, will lead to higher correlation coefficients.

from the resolved-scale strain rate field S_{ij}^Δ, requiring differentiation of the smallest-scale components u_i^Δ in the resolved velocity field. That study found errors arising from the discretization of the required derivatives which can exceed the magnitude of the subgrid stress τ_{ij}. This has been confirmed in other studies,[53] and has led to the use of very high-order finite-difference methods to reduce these truncation errors. By contrast, the multifractal subgrid-scale model derived here requires no explicit differentiation to evaluate the subgrid stress τ_{ij}^*, and thus will be comparatively less affected by discretization error.

While the present multifractal model does not require any such explicit differentiation, it does require the subtraction in (29) to determine the $u_i^\Delta(\mathbf{x},t)$ fields needed in (26). It is thus of interest to assess the numerical errors which this difference operation introduces in the model results. Power spectra were therefore calculated for the u_i^Δ and τ_{ij}^* fields obtained from the DNS data, and compared with corresponding spectra for their respective errors from the multifractal model.

Figure 17(a) shows the spectrum for the true u_i^Δ field calculated from the DNS data via (11) for $\alpha=2$, and the spectrum for the difference between this field and that obtained via (29). As is evident from these respective power spectra, the numerical errors made in calculating u_i^Δ are uniformly at least an order of magnitude smaller than the field values themselves over essentially the entire resolved range of scales. The result for τ_{ij}^* in (26) from the multifractal subgrid-scale model involves a rescaling of the u_i^Δ field to estimate u_i^{sgs}, and it is apparent from Fig. 17(a) that the underlying u_i^Δ field is relatively free of numerical errors.

Figure 17(b) shows an analogous comparison of the τ_{ij}^* spectrum obtained from the DNS data, and the corresponding

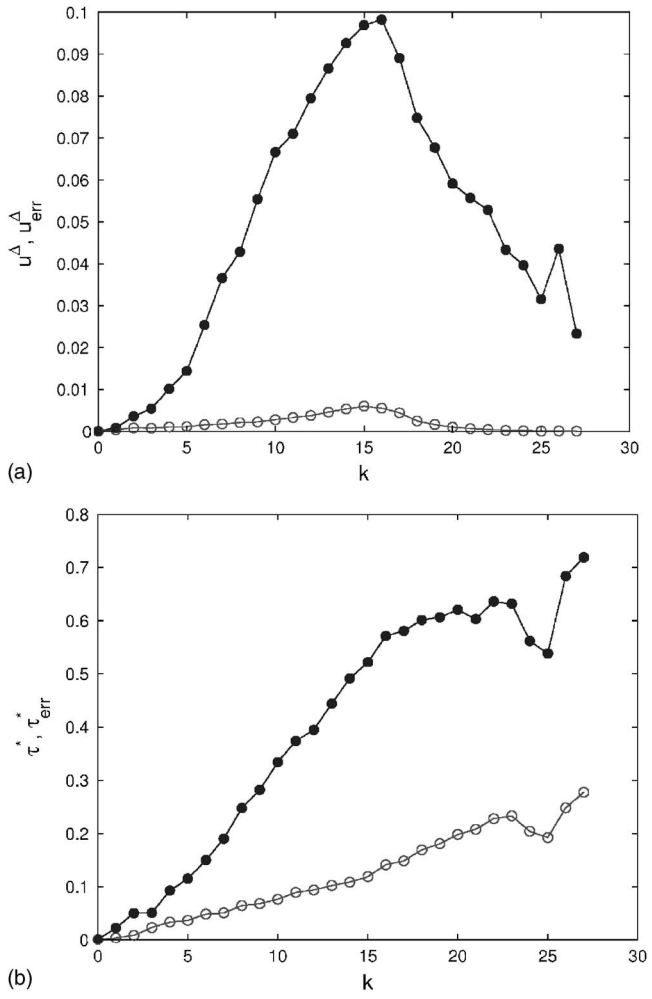

FIG. 17. Typical power spectra for (top) DNS value for u_i^Δ (solid) from (11) and $(u_i^\Delta)_{error}$ (open) from difference between model and DNS values in (29) and (11), and (bottom) DNS value for τ_{ij}^* (solid) from (5) and $(\tau_{ij}^*)_{error}$ (open) from difference between model and DNS values in (26) and (5). Note that relative error in u_i^Δ due to subtraction is much smaller than relative error in τ_{ij}^* due to model approximations, suggesting that model errors are dominated by present neglect of subgrid-subgrid correlations and not by numerical errors.

spectrum of the error in τ_{ij}^* obtained from the multifractal model. Here it is apparent that the relative error magnitudes are much larger, indicating that most of the errors in τ_{ij}^* from the multifractal model are due to the model itself, and not due to numerical errors in the u_i^Δ field supplied to the model from the resolved scales. Moreover, only at the largest resolved wave modes ($k \leqslant 5$) do the errors approach the τ_{ij}^* values themselves. These low wave number modes approach the scales at which the forcing of the turbulence in the simulation dominates the flow, and thus would not be captured by a subgrid-scale model based on inertial-range scalings.

Together these results suggest that the multifractal model is relatively insensitive to numerical errors introduced by the required difference in (29). This is further supported by results[34] from *a posteriori* evaluation of this approach to subgrid-scale modeling and large-eddy simulation, where the present subgrid-scale model is combined with a flow solver and used to assess the effect of numerical errors on the resulting filtered velocity field $\bar{u}_i(\mathbf{x},t)$.

VI. DISCUSSION AND CONCLUSIONS

This study has introduced a multifractal model for the subgrid-scale stresses in large-eddy simulation, and has evaluated the resulting model in *a priori* tests with filtered DNS data. For the subgrid-scale model developed here, the subgrid vorticity field is represented by a stochastic multifractal cascade in (14) that distributes the total subgrid enstrophy from the resolved scale Δ to the inner scale λ_ν by a scale-invariant multiplier distribution $P(\mathcal{M})$. This approach is motivated by experimental and computational evidence that has verified such multifractal scale-similarity over inertial-range length scales in gradient fields associated with turbulent flows. Consistent with this multiplicative cascade in the subgrid enstrophy field, the vorticity orientation in each of the inner-scale cells that comprise the subgrid vorticity field is related to the orientation of the vorticity at the resolved scale Δ by an additive cascade that produces increasingly isotropic decorrelation of the orientations from the resolved scale to the inner scale λ_ν. Note that correlations in both the subgrid enstrophy and orientation fields among the inner-scale cells within each resolved grid cell are implied by their respective cascades. For instance, half of all inner-scale cells share the same $\mathcal{M}_1$, one-quarter share the same $\mathcal{M}_2$, etc. In principle such correlations in the subgrid enstrophy field, as well as those in the subgrid orientation field, could be accounted for in evaluating the Biot–Savart integrals, which represent an obvious area for further improvement in the model. Assuming these correlations to be negligible leads to the expression in (23) for the expectation value of the subgrid velocities, and for the associated subgrid stresses in (26). The results in Figs. 8 and 9 suggest that neglecting these correlations still produces good representations for the filtered subgrid velocity components. The effect of these correlations becomes apparent, however, in Figs. 13 and 14, where it is evident that both of the resolved-subgrid interactions are accurately modeled but the subgrid-subgrid contribution is essentially zero. This in turn becomes the main contributor to the remaining errors in the subgrid stresses, though the subgrid energy production in Figs. 15 and 16 is nevertheless reasonably represented. An obvious path for extending the present subgrid-scale model is to account for the correlations produced by the cascades in the subgrid vorticity field to provide a better representation of the subgrid-subgrid interaction in (5).

Note that the result for τ_{ij}^* in (26) from the present multifractal subgrid-scale model is in practice no more computationally burdensome to implement than are corresponding forms for τ_{ij} from simple eddy-viscosity models. Unlike such eddy-viscosity models, however, the present model is based on a specific physical representation of the subgrid vorticity field that is strongly supported by theoretical, experimental, and computational evidence. In view of this physical basis, it is not surprising that in *a priori* tests the multifractal model produces correlations with the actual subgrid stresses and subgrid energy production that exceed the values commonly reported for eddy-viscosity models. It also provides similarly high correlations as have been reported for the scale-similarity model of Bardina *et al.*[14,15] commonly used in "mixed models" in conjunction with eddy-viscosity representations,[16] while at the same time providing much higher correlations for the subgrid energy production field $\mathcal{P}(\mathbf{x},t)$. Furthermore, unlike dynamic eddy-viscosity models, the present multifractal subgrid-scale model does not require explicit differentiation of the smallest-scale components in the resolved velocity field, and thus is relatively less affected by discretization errors, which in some models can lead to errors exceeding the subgrid stresses themselves.

The present multifractal subgrid-scale model is most closely related to the broad class of subgrid estimation approaches, since it is fundamentally based on estimation of a subgrid-scale field. Other models in this class include the velocity-estimation approach of Domaradzki and Loh[21] and the fractal-interpolation approach of Scotti and Meneveau.[22] The latter, however, is based on a specific assumed rule for estimating the subgrid velocity field, while the former is based on estimating the subgrid velocities using truncated Navier–Stokes dynamics on a finer grid. Unlike these direct estimates of the subgrid velocity field, the present multifractal subgrid-scale approach is based on estimation of the subgrid vorticity field, which makes use of the approach to isotropy at increasingly smaller scales and the multifractal scale-similarity of the subgrid enstrophy field.

The multifractal subgrid-scale model as formulated here requires, at least in principle, that the resolved-scale calculations reach at least into the large-scale end of the inertial range of scales, so that the inertial-range scaling that implicitly determines the total subgrid enstrophy remains valid. Related to this, since here equilibrium inertial-range scaling laws have been used to determine the total subgrid enstrophy via (12), the resulting momentum and energy transfer between resolved and subgrid scales might be expected to show increasing inaccuracy where local equilibrium departures are significant, as would be the case for all subgrid-scale models that make use of equilibrium inertial-range scalings. However, the present results at $Re_\Delta \approx 2550$, for which the resolved scale Δ coincides with the scales at which forcing is introduced in the DNS field, nevertheless show good agreement in the *a priori* tests, suggesting that the model may be more robust than the inertial-range assumption might suggest.

At low values of Re_Δ, the multifractal subgrid-scale model depends weakly on the number of cascade steps $\mathcal{N}$ in (10), and thus in principle requires knowing the local strain-limited viscous diffusion scale λ_ν.[56,57] This could be dynamically related to the local instantaneous magnitude of the resolved-scale strain rate $\mathcal{S} \equiv (\bar{S}_{ij}\bar{S}_{ij})^{1/2}$ and the viscosity ν. For $Re_\Delta \gg 1$, where $Re_\Delta \equiv \mathcal{S}\Delta^2/\nu$, significant self-induced stretching occurs within the subgrid vorticity field, and thus the strain rate at the smallest scale will be $\mathcal{S}_\nu = \mathcal{S}(\Delta/\lambda_\nu)^{2/3}$, with the resulting inner length scale $\lambda_\nu \sim (\nu/\mathcal{S}_\nu)^{1/2}$ giving the correct Kolmogorov-like scaling $\lambda_\nu/\Delta \sim Re_\Delta^{-3/4}$. The proportionality constant, denoted c_ν, will then be universal and allows λ_ν to be determined locally from the resolved strain rate $\mathcal{S}$. Similarly the model as formulated here could in principle be extended to account for near-wall effects. In particular, the reduction in Re_Δ leads to a decrease in the number of

cascade steps, and thereby to a higher degree of residual correlation in both the enstrophy and orientation fields. The strong anisotropy in near-wall turbulence will also lead to stronger correlations in the subgrid vorticity orientations. Such near-wall extensions of the present multifractal model are beyond the scope of this paper, but represent obvious areas for further development of this modeling approach.

A companion paper (Ref. 34) demonstrates the implementation of this multifractal subgrid-scale model in an LES flow solver, and examines the characteristics of the resolved-scale turbulence that result in *a posteriori* tests of the model and the flow solver.

ACKNOWLEDGMENTS

The authors gratefully acknowledge many helpful discussions with D. Dowling and K. Powell at Michigan. This work was jointly supported, in part, by the National Aeronautics and Space Administration (NASA) Marshall and Glenn Research Centers and the Department of Defense (DoD) within the NASA Constellation University Institutes Project (CUIP) Space Vehicle Technology Institute (SVTI) under Grant No. NCC3-989, with Claudia Meyer as the project manager. G.C.B. gratefully acknowledges the generous financial support of the François-Xavier Bagnoud Fellowship provided by the Association François-Xavier Bagnoud of Sion, Switzerland. The DNS data used in part of this study were generously provided by the Center for Turbulence Research (CTR) at Stanford University and the NASA Ames Research Center, Moffet Field, California.

[1] W. C. Reynolds, "The potential and limitations of direct and large eddy simulations," in *Whither Turbulence? Turbulence at the Crossroads*, Lecture Notes in Physics, edited by J. L. Lumley (Springer-Verlag, Berlin, 1990), Vol. 357.
[2] J. Smagorinsky, "General circulation experiments with the primitive equations: I. The basic equations," Mon. Weather Rev. **91**, 99 (1963).
[3] P. Moin, "Advances in large eddy simulation methodology for complex flows," Int. J. Heat Fluid Flow **23**, 710 (2002).
[4] J. Jimenez, "Computing high-Reynolds-number turbulence: Will simulations ever replace experiments?" J. Turbul. **4**, 022 (2003).
[5] P. Sagaut, *Large-Eddy Simulation for Incompressible Flow* (Springer-Verlag, Berlin, 2002).
[6] L. F. Richardson, *Weather Prediction by Numerical Process* (Cambridge University Press, Cambridge, 1922).
[7] M. Germano, U. Piomelli, P. Moin, and W. H. Cabot, "A dynamic subgrid-scale eddy viscosity model," Phys. Fluids A **3**, 1760 (1991).
[8] S. Ghosal, T. S. Lund, P. Moin, and K. Akselvoll, "A dynamic localization model for large-eddy simulation of turbulent flows," J. Fluid Mech. **286**, 229 (1995).
[9] U. Piomelli and J. H. Liu, "Large-eddy simulation of rotating channel flows using a localized dynamic-model," Phys. Fluids **7**, 839 (1995).
[10] C. Meneveau, T. Lund, and W. Cabot, "A Lagrangian dynamic subgrid-scale model of turbulence," J. Fluid Mech. **319**, 353 (1996).
[11] E. Bou-Zeid, C. Meneveau, and M. Parlange, "A scale-dependent Lagrangian dynamic model for large eddy simulation of complex turbulent flows," Phys. Fluids **17**, 025105 (2005).
[12] R. Kraichnan, "Eddy viscosity in two and three dimensions," J. Atmos. Sci. **65**, 575 (1976).
[13] O. Métais and M. Lesieur, "Spectral large-eddy simulation of isotropic and stably stratified turbulence," J. Fluid Mech. **239**, 157 (1992).
[14] J. Bardina, J. H. Ferziger, and W. C. Reynolds, "Improved subgrid models for large eddy simulation," AIAA Paper 80-1357 (AIAA, Washington, D.C., 1980).
[15] J. Bardina, J. H. Ferziger, and W. C. Reynolds, "Improved turbulence models based on large eddy simulation of homogeneous, incompressible, turbulent flows," Technical Report TF-19, Thermosciences Division, Stanford University, Stanford, CA (1983).
[16] Y. Zang, R. L. Street, and J. Koseff, "A dynamic mixed subgrid-scale model and its application to turbulent recirculating flows," Phys. Fluids A **5**, 3186 (1993).
[17] J. G. Brasseur and C. H. Wei, "Interscale dynamics and local isotropy in high Reynolds number turbulence within triadic interactions," Phys. Fluids **6**, 842 (1994).
[18] B. J. Geurts, "Inverse modeling for large-eddy simulation," Phys. Fluids **9**, 3585 (1997).
[19] S. Stoltz and N. A. Adams, "An approximate deconvolution procedure for large-eddy simulation," Phys. Fluids **11**, 1699 (1999).
[20] J. A. Domaradzki and E. M. Saiki, "A subgrid-scale model based on the estimation of unresolved scales of turbulence," Phys. Fluids **9**, 2148 (1997).
[21] J. A. Domaradzki and K. Loh, "The subgrid-scale estimation model in the physical space representation," Phys. Fluids **11**, 2330 (1999).
[22] A. Scotti and C. Meneveau, "A fractal model for large eddy simulation of turbulent flow," Physica D **127**, 198 (1999).
[23] D. I. Pullin and P. G. Saffman, "Reynolds stresses and one-dimensional spectra for a vortex model of homogeneous anisotropic turbulence," Phys. Fluids **6**, 1787 (1994).
[24] A. Misra and D. I. Pullin, "A vortex-based subgrid stress model for large eddy simulation," Phys. Fluids **9**, 2443 (1997).
[25] J. Mansfield, O. Knio, and C. Meneveau, "A dynamic LES scheme for the vorticity transport equation: Formulation and a priori tests," J. Comput. Phys. **145**, 693 (1998).
[26] M. Farge, K. Schneider, and N. Kevlahan, "Non-Gaussianity and coherent vortex simulation for two-dimensional turbulence using an adaptive orthogonal wavelet basis," Phys. Fluids **11**, 2187 (1999).
[27] J. W. Deardorff, "A numerical study of three-dimensional turbulent channel flow at large Reynolds numbers," J. Fluid Mech. **41**, 453 (1970).
[28] A. Leonard, "Energy cascade in large-eddy simulations of turbulent fluid flows," Adv. Geophys. **18A**, 237 (1974).
[29] R. A. Clark, J. H. Ferziger, and W. C. Reynolds, "Evaluation of subgrid-scale models using an accurately simulated turbulent flow," J. Fluid Mech. **91**, 1 (1979).
[30] G. S. Winckelmans, A. A. Wray, O. V. Vasilyev, and H. Jeanmart, "Explicit-filtering large-eddy simulation using the tensor-diffusivity model supplemented by a dynamic Smagorinsky term," Phys. Fluids **13**, 1385 (2001).
[31] C. Meneveau and K. R. Sreenivasan, "Simple multifractal cascade model for fully developed turbulence," Phys. Rev. Lett. **59**, 1424 (1987).
[32] C. Meneveau and K. R. Sreenivasan, "The multifractal nature of turbulent energy dissipation," J. Fluid Mech. **224**, 429 (1991).
[33] K. R. Sreenivasan, "Fractals and multifractals in fluid turbulence," Annu. Rev. Fluid Mech. **23**, 539 (1991).
[34] G. C. Burton and W. J. A. Dahm, "Multifractal subgrid-scale modeling for large-eddy simulation. II. Backscatter limiting and *a posteriori* evaluation," Phys. Fluids **17**, 075112 (2005).
[35] K. Falconer, *Fractal Geometry: Mathematical Foundations and Applications* (Wiley, New York, 1990).
[36] H. Peitgen, H. Jurgen, and D. Saupe, *Chaos and Fractals: New Frontiers of Science* (Springer-Verlag, Berlin, 1992).
[37] C. Meneveau, "Analysis of turbulence in the orthonormal wavelet representation," J. Fluid Mech. **232**, 469 (1991).
[38] K. R. Sreenivasan and G. Stolovitzky, "Turbulent cascades," J. Stat. Phys. **78**, 311 (1995).
[39] R. R. Prasad, C. Meneveau, and K. R. Sreenivasan, "The multifractal nature of the dissipation field of passive scalars in fully turbulent flows," Phys. Rev. Lett. **61**, 74 (1988).
[40] K. R. Sreenivasan and R. R. Prasad, "New results on the fractal and multifractal structure of the large Schmidt number passive scalars in fully turbulent flows," Physica D **38**, 322 (1989).
[41] R. D. Frederiksen, W. J. A. Dahm, and D. R. Dowling, "Experimental assessment of fractal scale similarity in turbulent flows. Part 3. Multifractal scaling," J. Fluid Mech. **338**, 127 (1997).
[42] R. D. Frederiksen, W. J. A. Dahm, and D. R. Dowling, "Experimental assessment of fractal scale similarity in turbulent flows. Part 4. Effects of Reynolds and Schmidt numbers," J. Fluid Mech. **377**, 169 (1998).
[43] A. B. Chhabra and K. R. Sreenivasan, "Scale-invariant multiplier distributions in turbulence," Phys. Rev. Lett. **68**, 2762 (1992).
[44] G. C. Burton, "A multifractal subgrid-scale model for large-eddy simulation of turbulent flows," Ph.D. dissertation, The University of Michigan, Ann Arbor, Michigan (2003).

[45] J. A. Mullin and W. J. A. Dahm, "Dual-plane stereo particle image velocimetry measurements of velocity gradient tensor fields in turbulent shear flow. Part 2: Experimental results," Phys. Fluids (submitted).
[46] S. Liu, C. Meneveau, and J. Katz, "On the properties of similarity subgrid-scale models as deduced from measurements in a turbulent jet," J. Fluid Mech. **275**, 83 (1994).
[47] J. A. Langford and R. D. Moser, "Optimal LES formulations for isotropic turbulence," J. Fluid Mech. **398**, 321 (1999).
[48] U. Piomelli, W. H. Cabot, P. Moin, and S. Lee, "Subgrid-scale backscatter in turbulent and transitional flows," Phys. Fluids A **3**, 1766 (1991).
[49] D. Carati, G. S. Winckelmans, and H. Jeanmart, "On the modeling of the subgrid-scale and filtered stress tensors in large-eddy simulation," J. Fluid Mech. **441**, 119 (2001).
[50] J. Jimenez, A. A. Wray, P. G. Saffman, and R. S. Rogallo, "The structure of intense vorticity in isotropic turbulence," J. Fluid Mech. **255**, 65 (1993).
[51] S. Ghosal, "An analysis of numerical errors in large-eddy simulations of turbulence," J. Comput. Phys. **125**, 187 (1996).
[52] S. Ghosal, "Mathematical and physical constraints on large-eddy simulation of turbulence," AIAA J. **37**, 425 (1999).
[53] A. G. Kravchenko and P. Moin, "On the effect of numerical errors in large eddy simulations of turbulent flows," J. Comput. Phys. **131**, 310 (1997).
[54] C. Fureby and G. Tabor, "Mathematical and physical constraints on large-eddy simulations," Theor. Comput. Fluid Dyn. **9**, 85 (1997).
[55] F. K. Chow and P. Moin, "A further study of numerical errors in large-eddy simulations," J. Comput. Phys. **184**, 366 (2003).
[56] K. A. Buch and W. J. A. Dahm, "Experimental study of the fine-scale structure of conserved scalar mixing in turbulent shear flows. Part 1. $Sc \gg 1$," J. Fluid Mech. **317**, 21 (1996).
[57] K. A. Buch and W. J. A. Dahm, "Experimental study of the fine-scale structure of conserved scalar mixing in turbulent shear flows. Part 2. $Sc \approx 1$," J. Fluid Mech. **364**, 1 (1998).